$Tm^{3+}:Y_2O_3$ investigated for a quantum light storage application

T. Chanelière, J. Ruggiero, and J.-L. Le Gouët
Laboratoire Aimé Cotton, CNRS-UPR 3321, Université Paris-Sud, Bâtiment 505, 91405 Orsay Cedex, France

W. Tittel
Institute for Quantum Information Science, University of Calgary, 2500 University Drive NW, Calgary, Alberta, Canada T2N 1N4

J.-H. Mun, A. Jouini, and A. Yoshikawa
Division of Physical Process Design, Institute of Multidisciplinary Research for Advanced Materials (IMRAM), Tohoku University, 2-1-1 Katahira, Aoba-ku, Sendai, 980-8577, Japan

G. Boulon
Physical Chemistry of Luminescent Materials, University Claude Bernard Lyon 1, CNRS UMR 5620, 69622 Villeurbanne Cedex, France

Y. Le Du, Ph. Goldner, F. Beaudoux, J. Vincent, E. Antic-Fidancev, and O. Guillot-Noël
Laboratoire de Chimie de la Matière Condensée de Paris, CNRS-UMR 7574, Ecole Nationale Supérieure de Chimie de Paris (ENSCP), 11 rue Pierre et Marie Curie, 75231 Paris Cedex 05, France

(Received 13 March 2008; published 20 June 2008)

In this paper, we investigate a new medium for quantum light storage in crystals. Indeed, $Tm^{3+}:Y_2O_3$ exhibits all the features that are currently considered crucial for a storage protocol. First, optical measurements confirm our crystal-field analysis. Then, we explain how to tailor a three-level Λ system and ultimately measure the Stark coefficient in this material. To our knowledge, these properties have not been investigated at the same time in a thulium based crystal, for which both the operating wavelength and an adjustable storage bandwidth are significant assets that other rare-earth ions lack.

DOI: 10.1103/PhysRevB.77.245127 PACS number(s): 03.67.−a, 32.60.+i, 32.70.Cs, 32.80.Qk

I. INTRODUCTION

The design of a solid-state quantum light memory has been recently considered in rare-earth-ion–doped crystals. These materials historically first aroused interest because of their population lifetime, which is still the basis in laser applications. Later, coherent effects were also widely studied for classical light storage and more generally for optical data processing benefiting from the long lifetime of the atomic coherences in these crystals. Now quantum light storage raises different problems, and this is why it is useful to reconsider the catalog of rare-earth-ion–doped crystals from a different point of view.

The ideal properties of a quantum memory material strongly depend on the storage protocol used. Nevertheless, they usually rely on a few common characteristics that we can briefly review. The most promising protocols can be split into two categories. First, the electromagnetically induced transparency (EIT) based ones, where the state of light is directly converted into Raman coherences.[1] Guided by the stopped-light experiment—proposed and first verified for atomic gases—this category of quantum protocols should be easily applied to rare-earth-doped crystals as soon as a relatively long lifetime of the Raman coherence is observed. Classical light storage has been experimentally demonstrated for praseodymium in yttrium orthosilicate.[2] Second, rephasing protocols have emerged and are now considered as very promising. They are indeed in the direct lineage of the coherent transient phenomena that have been studied for decades.[3] The rephasing process cannot be solely based on the usual photon echo techniques: the population inversion intrinsically associated with the coherence rephasing would spoil the memory retrieval because of the detrimental fluorescence. A gentle way to rephase the coherences is to prepare the medium absorption profile by controlling reversible inhomogeneous broadening.[4–6] The broadening reversal generates an echo, which can be the exact copy of the incoming signal. The frequency detuning is usually controlled by applying an external electric field and thus relies on the linear Stark effect. This was recently investigated experimentally using different configurations.[5,7,8] To change the direction of echo retrieval, coherent light pulses may need to be applied on an auxiliary transition, which also requires long-lived Raman coherences, similar to the EIT based approach to quantum state storage.

Taking into account these two categories of quantum memory protocols, two important features of a promising material candidate for quantum storage are the ability to optically control the ground-state coherence (Raman transition) and the presence of a linear Stark effect. Our goal here is to show that $Tm^{3+}:Y_2O_3$ can fulfill these two criteria. We would like to emphasize that the simple energy-level structure of Tm^{3+} ions—somewhat unusual among the rare-earth ions—is advantageous. Because of the $I=1/2$ nuclear spin, there is no hyperfine structure in the absence of an external magnetic field. This seems to restrict Tm^{3+} to a purely optical two-level system or at least to a certain level of poverty for any ground-state coherence addressing. Applying an external magnetic field removes the nuclear-spin degeneracy and splits the electronic levels. A three-level Λ system with

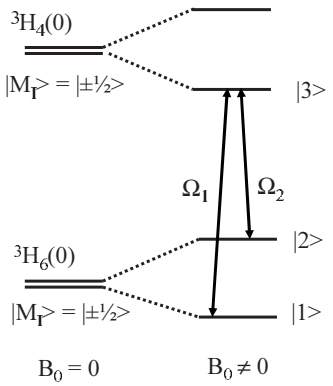

FIG. 1. Three-level Λ system in the case of Tm^{3+} ions between three hyperfine levels of the first crystal-field states of the $^3H_6$ and $^3H_4$ multiplets. The external magnetic field B_0 lifts the nuclear-spin degeneracy and can induce different M_I mixing in the ground and excited states.

Tm^{3+} ions (Fig. 1) involves the two hyperfine levels of the ground state $^3H_6(0)$ and one hyperfine level of the excited state $^3H_4(0)$.

Even when an external magnetic field lifts the degeneracies of the ground and excited states, a nuclear Zeeman based Λ system cannot be optically controlled because nuclear-spin flipping is, in principle, optically forbidden. However, for Tm^{3+}-doped yttrium aluminum garnet (YAG), we recently showed, both theoretically[9] and experimentally,[10,11] that this selection rule can be overcome. Under particular orientations of the external magnetic field, the coupling of the electronic Zeeman and hyperfine interactions relaxes the selection rule and makes possible the optical addressing. In this paper, we make use of this property to propose the building of an efficient three-level system in $Tm^{3+}:Y_2O_3$. The yttrium oxide host is not simply a substitute for Tm:YAG. Indeed, the D_2 site symmetry of thulium in YAG forbids any permanent electric dipole. On the contrary, the C_2 site symmetry in yttrium oxide allows a linear Stark effect, whose coefficient is measured in this work.

The convenience of the operating wavelength (795 nm) for Tm^{3+} is particularly interesting in comparison with that for Pr^{3+} (606 nm), even though the latter exhibits a Λ system based on the hyperfine structure without any external magnetic field. Our system also benefits from the possibility of controlling the ground-state splitting by adjusting the magnetic-field intensity. Indeed, this should allow us to increase at will the bandwidth of the memory. Finally, it is worth noting that Tm^{3+} also has a $^3F_4$ shelving state. Far-off-resonance population transfer is a necessary preliminary step common to many storage protocols. The latter point enforces the interest in thulium-doped crystals for quantum memory application.

Our paper is organized as follows: We first give the general features of $Tm^{3+}:Y_2O_3$ and define the different site orientations in the crystallographic frame. We then determine theoretically the proper orientations of the magnetic field to efficiently excite the ground-state coherences. We finally show experimentally the static electric-field sensitivity and measure the linear Stark coefficient. To our knowledge, these two crucial properties have never been considered at the same time in a thulium-doped crystal.

II. GENERAL FEATURES AND CRYSTAL-FIELD ANALYSIS

The trivalent thulium has a 12 electron configuration and is thus a non-Kramers ion.[12] The transition we are looking at, from the $^3H_6$ to the $^3H_4$ levels, lies in the near infrared (795 nm) accessible with laser diodes and is then particularly convenient. In between these levels, $^3H_4$ relaxes toward $^3H_5$ (submillisecond time scale), which rapidly decays to the $^3H_4$ metastable state (10 ms lifetime typically).

Yttrium oxide Y_2O_3 is a cubic crystal with 16 f.u./elementary cell. Among the 32 yttrium cations, 8 occupy a C_{3i} point site symmetry and 24 a C_2 one. The trivalent thulium substitutes for yttrium in both sites. We shall consider only the C_2 sites which can be observed optically. The local crystal-field axes (x,y,z) of the C_2 sites are parallel to the crystallographic frame [1 0 0], [0 1 0], and [0 0 1] axes. This will radically simplify the crystal-field analysis and the physical interpretation of the experiment under static electric and magnetic fields.

The lack of hyperfine structure in the absence of an external magnetic field is caused by the $I=1/2$ nuclear spin. The $^3H_6(0)$ to $^3H_4(0)$ transition between the two lower states of the multiplets is then a pure two-level system for coherent transient applications. The $^3H_4$ metastable state can be used for storing population in hole-burning experiments.

For Tm^{3+} ions in a low site symmetry C_2, the spin Hamiltonian H_{SH} is given in a J multiplet by

$$H_{SH} = \mathbf{B}\cdot(-\beta^2 g_J^2 \mathbf{\Lambda})\cdot\mathbf{B} + \mathbf{B}\cdot(-g_n\beta_n \mathbf{Id} - 2g_J\beta\mathbf{\Lambda})\cdot\mathbf{I}, \tag{1}$$

where β and β_n are the electronic and nuclear Bohr magnetons, g_J is the g factor associated with the J multiplet, and g_n is the nuclear g factor of Tm^{3+}. $\mathbf{I}$ is the nuclear-spin operator. $\mathbf{Id}$ is the identity operator. The $\mathbf{\Lambda}$ tensor in H_{SH} is determined by second-order perturbation theory and is calculated by taking into account all the crystal-field levels of a particular J multiplet,

$$\Lambda_{\alpha\beta} = \sum_{n\neq 0} A_J \frac{\langle 0|J_\alpha|n\rangle\langle n|J_\beta|0\rangle}{E_n - E_0}, \tag{2}$$

where α and β stand for x, y, or z. A_J is the hyperfine constant for the J multiplet. The index 0 denotes the first crystal-field level [$^3H_6(0)$ or $^3H_4(0)$] and n the other crystal-field levels of a $^{2S+1}L_J$ multiplet. E_n is the energy of the crystal-field level n. In a C_2 symmetry, $\mathbf{\Lambda}$ in the local crystal-field frame (x,y,z) takes the following form:

$$\mathbf{\Lambda} = \begin{pmatrix} \Lambda_{xx} & \Lambda_{xy} & 0 \\ \Lambda_{xy} & \Lambda_{yy} & 0 \\ 0 & 0 & \Lambda_{zz} \end{pmatrix}. \tag{3}$$

Equation (1) clearly shows that the coupling of the electronic Zeeman with the hyperfine interaction $(2g_J\beta\Lambda)$ is responsible for the hyperfine splittings. Because the hyperfine term

$\Lambda_{\alpha\beta}$ is strongly dependent on the crystal-field splitting of the J multiplet [Eq. (2)], we obtain different hyperfine splittings for the ground state $^3H_6(0)$ and the excited state $^3H_4(0)$. In Eq. (1), the first term on the right-hand side $[\mathbf{B}\cdot(-\beta^2 g_J^2 \mathbf{\Lambda})\cdot\mathbf{B}]$ leads to a global shift of all the hyperfine transitions in a given J multiplet independently of the nuclear-spin projection M_I. From now on, this term will not be considered and we shall work with this simplified spin-Hamiltonian,

$$H'_{SH} = \mathbf{B}\cdot\gamma\cdot\mathbf{I}, \tag{4}$$

where γ is a pseudonuclear tensor given by

$$\gamma = -g_n\beta_n\mathbf{Id} - 2g_J\beta\mathbf{\Lambda}. \tag{5}$$

As we already demonstrated previously,[9] for a given magnetic-field orientation, these different hyperfine splittings lead to different M_I mixings at the $^3H_6(0)$ and $^3H_4(0)$ levels: this relaxes the selection rule on the nuclear-spin projection. An efficient three-level Λ system can thus be obtained and the branching ratio R between the two optical transitions defined in Fig. 3 is calculated from the nuclear part of the wave functions as

$$R = \frac{|\langle 2|3\rangle|^2}{|\langle 1|3\rangle|^2}. \tag{6}$$

Because the whole wave function can be split into an electronic and a nuclear part,[9] the branching ratio R then requires the computation of the wave functions. This is done through the diagonalization of the spin Hamiltonian whose parameters are computed from crystal-field calculations. The full Hamiltonian H_F is given by

$$H_F = H_{FI} + H_{CF}, \tag{7}$$

where H_{FI} is the free-ion Hamiltonian and H_{CF} is the crystal-field one. The free-ion interactions are written according to the formalism of Carnall *et al.*,[13]

$$H_{FI} = H_0 + \sum_{k=1,2,3} E^k e_k + \zeta_{4f} A_{SO} + \alpha L(L+1) + \beta G(G_2) + \gamma G(R_7) + \sum_{i=2,3,4,6,7,8} t_i T^i. \tag{8}$$

In this expression, H_0 is the spherical symmetric one-electron part of the Hamiltonian, E^k are the Racah parameters, and ζ_{4f} is the spin-orbit coupling constant. Here e_k and A_{SO} represent the angular parts of the electrostatic repulsion and the spin-orbit coupling, respectively. The α, β, and γ parameters are associated with the two-body interactions and the T^i (Judd parameters) with the three-body interactions. $G(G_2)$ and $G(R_7)$ are the eigenvalues of Casimir's operators for the groups G_2 and R_7.[14] The Judd parameters are vanishing for the f^2 and f^{12} configurations. Other interactions such as spin-spin and spin-other orbit interactions operating through the M^k and P^k parameters are not included in the calculations. Following Wybourne's formalism,[14] the crystal-field Hamiltonian is expressed as a sum of products of crystal-field parameters and spherical harmonics Y_{kq},

TABLE I. Free-ion and crystal-field parameters for Tm^{3+} ions in Y_2O_3 single crystals (in cm^{-1}) and experimental and calculated energy levels (in cm^{-1}) corresponding to the two $^3H_6$ and $^3H_4$ multiplets of interest in this work. The rms standard deviation σ is indicated.

Parameter	(cm^{-1})	Multiplet $^{2S+1}L_J$	Energy levels (cm^{-1}) Expt.	Calc.
E^0	17 785	$^3H_6$	0	0
E^1	6 836		31	35.1
E^2	33.2		89	94.2
E^3	651		219	216.1
α	6.5		230	230.1
β	−659		340	354.1
γ	750		382	393
ζ_{4f}	2 612.6		436	434.1
B_0^2	−192.6		488	479.6
B_0^4	−1 048.5			647.6
B_0^6	444.6		692	684.1
B_2^2	−516.9		788	783.8
B_2^4	−1073.5		797	790.6
B_4^4	697			
B_2^6	12.5			
B_4^6	460	$^3H_4$	12 556	12 532.2
B_6^6	66.2		12 634	12 630.9
S_2^4	439		12 697	12 676.1
S_4^4	−594		12 813	12 795.5
S_2^6	−161		12 842	12 843.3
S_4^6	−172		12 872	12 864.2
S_6^6	−80			12 918.8
			13 017	13 050.4
σ	18.6		13 048	13 062.5

$$H_{CF} = \sum_{k=2}^{4,6}\sum_{q=0}^{k}\{B_q^k[C_q^{(k)} + (-1)^q C_{-q}^{(k)}] + iS_q^k[C_q^{(k)} - (-1)^q C_{-q}^{(k)}]\}, \tag{9}$$

with

$$C_q^{(k)} = \sqrt{\frac{4\pi}{2k+1}}Y_{kq}. \tag{10}$$

The number of nonzero crystal-field parameters B_q^k and S_q^k, real and imaginary parts, depends on the site symmetry of the lanthanide ion in the structure.

The energy levels, determined by Leavitt *et al.*[12] from absorption and emission measurements, are used to calculate the parameters of the free-ion and crystal-field Hamiltonians. For the free-ion Hamiltonian, eight parameters were varied, i.e., E^0, E^1, E^2, and E^3 Racah parameters; α, β, and γ Trees parameters; and ζ_{4f}. The C_2 crystal-field parameters involve nine nonzero real B_q^k crystal-field parameters, namely, B_0^2, B_0^4, B_0^6, B_2^2, B_2^4, B_4^4, B_2^6, B_4^6, and B_6^6, and five nonzero real S_q^k crystal-field parameters, namely, S_2^4, S_4^4, S_2^6, S_4^6, and S_6^6. The

TABLE II. Spin-Hamiltonian parameters of the first crystal-field states of the $^3H_6$ and $^3H_4$ multiplets.

Parameter	Crystal-field level	
	$^3H_6(0)$	$^3H_4(0)$
g_J	1.16	0.95
A_J (MHz)	−470.3	−678.3
Λ_{xx}	-2.5×10^{-3}	-1.2×10^{-3}
Λ_{yy}	-2.7×10^{-4}	-2.3×10^{-4}
Λ_{zz}	-9.7×10^{-3}	-1.8×10^{-3}
Λ_{xy}	-6.6×10^{-4}	-1.4×10^{-4}
γ_{xx} (kHz/G)	8.57	3.51
γ_{yy} (kHz/G)	1.24	0.96
γ_{zz} (kHz/G)	32.12	5.22
γ_{xy} (kHz/G)	2.16	0.37

simulation of the energy-level scheme is performed on 59 experimental levels among the 91 possible of the $4f^{12}$ configuration. With a starting set of phenomenological free-ion and crystal-field parameters taken from the work of Leavitt *et al.*,[12] the rms standard deviation σ, taken as the figure of merit for the simulation, decreases to a rather good final value of 18.6 cm^{-1}. Table I gathers the free-ion and crystal-field parameters for Tm^{3+} ions in Y_2O_3 single crystals and the experimental and calculated energy levels of the $^3H_6$ and $^3H_4$ multiplets. The rms standard deviation is given for the 59 experimental levels. The full Hamiltonian (H_F) leaves each electronic level as a nondegenerate singlet due to the low point site symmetry of Tm^{3+} ions in the Y_2O_3 host.

From the crystal-field calculations, the spin-Hamiltonian parameters were calculated using Eqs. (2) and (5) and are gathered in Table II for the $^3H_6(0)$ and $^3H_4(0)$ states. Because the off-diagonal term γ_{xy} is different between the $^3H_6(0)$ and $^3H_4(0)$ states, the principal axes of the γ tensors do not have the same orientation in the ground and excited states. This will be particularly important in Sec. III, where we discuss the magnetic nonequivalency of the C_2 sites with regard to the external magnetic-field orientation.

From the spin-Hamiltonian parameters, we calculated R from Eq. (6). In the local crystal-field frame (x,y,z), the maximum value of $R=0.29$ is reached for an orientation of the external magnetic field of $\theta=87.3°$ or 92.7° and $\phi=101.5°$ in spherical coordinate with θ as the angle between the magnetic field and the local z axis and ϕ as the angle in the local xy plane. We shall see in Sec. III that if we take into account other optimization criteria than the simple maximization of R, i.e., the least number of magnetically nonequivalent sites and the orientation of the electric dipole moment of the transition, then the optimal (θ,ϕ) orientation will differ from the previously calculated one.

The orientation of the electric dipole moment of the $^3H_6(0)\rightarrow{}^3H_4(0)$ transition—as well as the one of the permanent dipole in the ground $^3H_6(0)$ and excited $^3H_4(0)$ states—can be retrieved from the electronic wave functions obtained from the diagonalization of H_F. Due to the C_2 symmetry, the only non-null B_q^k and S_q^k crystal-field parameters correspond to even k and q values. This implies that only two different

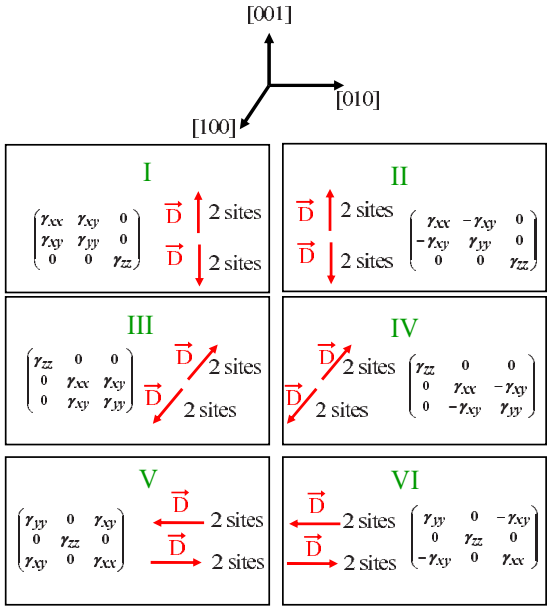

FIG. 2. (Color online) Representation of the six (I–VI) different magnetic nonequivalent classes in Y_2O_3. [100], [010], and [001] are the crystallographic directions. Associated with each class is the matrix representation of the pseudonuclear tensor γ. We also display the electric dipole moment $\vec{D}$ direction for all sites in each class. For example, classes I and II are magnetically nonequivalent for a general orientation of the external magnetic field. For class I, two of the four sites have a dipole moment $\vec{D}$ along the positive [001] direction and the other two along the negative [001] direction.

electronic wave functions of the type $\Sigma_{M_J}c_{M_J}|^{2S+1}L_J,2M_J\rangle$ or $\Sigma_{M_J}c_{M_J}|^{2S+1}L_J,2M_J+1\rangle$ corresponding to two different irreducible representations can be obtained. The crystal-field calculations give the same type of wave functions for the $^3H_6(0)$ and $^3H_4(0)$ states of the form $\Sigma_{M_J}c_{M_J}|^{2S+1}L_J,2M_J\rangle$. Using the fact that the $\hat{x}$, $\hat{y}$, and $\hat{z}$ electric dipole operators transform like the J_x, J_y, and J_z operators, respectively, and knowing that the only operator which does not change the type of electronic wave function is J_z, we conclude that the electric dipole moment of the $^3H_6(0)\rightarrow{}^3H_4(0)$ lies along the local z axis of the crystal-field frame. Because we are also interested in the effect of a static electric field (Stark effect), we note that the preceding argument also implies that the orientation of the permanent dipole in the ground and excited states will be carried by the local z axis.

The 24 sites of C_2 symmetry in the Y_2O_3 unit cell transform into one another according the symmetry operations of the host. This gives rise to different orientations of the local crystal-field frame leading to magnetic and electric nonequivalencies as a function of the orientation of the external magnetic and electric fields, respectively.

Now, for a general orientation of the external magnetic field, the 24 possible sites are equally distributed in six magnetically nonequivalent classes labeled I–VI with four sites per class. In Fig. 2, we have depicted the latter six classes together with their corresponding electric dipole moment orientations for the $^3H_6(0)\rightarrow{}^3H_4(0)$ transition. Classes I and II have their electric dipole moments oriented along the [001] direction, those of classes III and IV along the [100] direc-

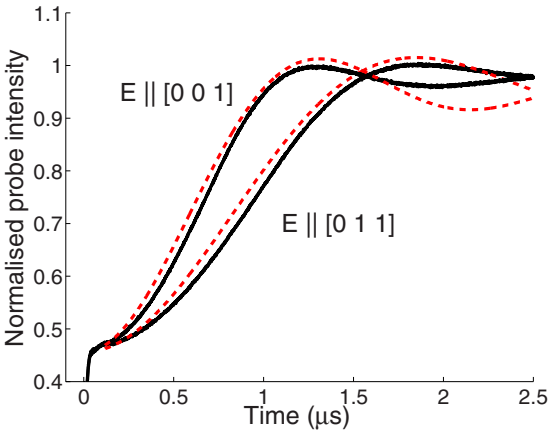

FIG. 3. (Color online) Optical nutation for two different orientations of the polarization: [001] and [011]. The extra damping of the Bessel-type oscillation could be explained by a short dephasing time for this specific temperature (around 4 μs at 3 K—see Sec. V for details).

tion, and those of classes V and VI along the [010] direction.

A simple way to check the orientation of the electric transition dipole is to perform an optical nutation experiment. This is not only a robust way to measure the absolute value of the Rabi frequency but, indeed, when multiple sites are present, it also allows us to distinguish and optically select the different dipole orientations. These nutation signals for various field polarizations are then strongly related to the crystal symmetry[15] as we shall show experimentally.

Our sample is a 0.15% doped $Tm^{3+}:Y_2O_3$ crystal made by micropulling down method.[16] For the growth, we use a rhenium crucible (46 mm in height and 36 mm in diameter) and the assembly was placed in hot zirconia ceramic. A 2 mm distance is kept between crucible and ceramic to prevent reaction. The crucible was heated inductively at a frequency of 20 kHz. The starting materials were prepared from high-purity commercial powders of Y_2O_3 (>99.99%) and Tm_2O_3 (99.99%). A single-crystal rod was used as a seed. The growth atmosphere is a mixture of Ar+3%H_2. The crystal length in the propagation direction is around 4 mm. It is oriented and cut along the crystallographic axes [100], [010], and [001]. The three axes being completely equivalent, we define the propagation axis as [100]. Then the polarization of the field is in the plane ([010], [001]). The sample is placed in liquid helium cryostat and cooled down to a few Kelvins. The peak absorption wavelength of the $^3H_6(0)$ to $^3H_4(0)$ transition is 796.514 nm with an inhomogeneous linewidth of 6 GHz. The absorption coefficient is around 2 cm^{-1} and the sample features optical coherence times of 4 μs at 3 K and 9 μs at 1.2 K, in good agreement with what was previously reported by Sun[17] (see Sec. V).

To confirm the sites orientation, we then performed an optical nutation experiment. Our measurements are in good agreement with the predicted orientation of the dipoles (see Fig. 2). For illustration, we plot in Fig. 3 two specific signals for a field polarization parallel to [001] and [011] with the laser propagating along [100].

In the first case, we address the sites with $\vec{D}$ parallel to [001] (sites of classes I and II in Fig. 2, these classes being equivalent in the absence of any magnetic field), which have the same transition dipole with a maximum Rabi frequency. For the latter field polarization (parallel to [011]), we address both sites with $\vec{D}$ parallel to [010] (sites of classes V and VI in Fig. 2) and $\vec{D}$ parallel to [001], but both with a Rabi frequency reduced by the $\sqrt{2}/2$ projection factor. The difference between the two curves in Fig. 3 is then a pure geometric effect (projection of the polarization). Any polarization angle between [001] and [010] would produce a composite nutation signal involving two sets of sites (classes I and II) and (classes V and VI) with frequencies given simply by the projection angle: this is experimentally observed. Although this measurement is simple, it supports our crystal-field analysis and gives an optical confirmation of the electric dipole orientation together with an appraisal of the crystalline quality of our sample.

III. OPTIMIZATION OF THE MAGNETIC-FIELD ORIENTATION

The optimization of the external magnetic-field orientation is meant to simultaneously satisfy the following con-

TABLE III. Magnetic-field orientation in the crystallographic frame simultaneously achieving a high branching ratio and a high absorption. Only two classes are then magnetically equivalent (good classes). The other classes, with poor R values (bad classes), are switched off by choosing a particular laser polarization E.

Magnetic-field orientation	Good classes		Bad classes		
(θ,ϕ) (deg)	Type	R	Type	R	Extinction
(86.8,90)					
(93.2,90)	I, II	0.13	III, IV, V, VI	$<5\times10^{-3}$	E// [001]
(90,90) (// [010])	I, II	0.12	III, IV, V, VI	$<5\times10^{-3}$	E// [001]
(3.2,0)					
(−3.2,0)	III, IV	0.13	I, II, V, VI	$<5\times10^{-3}$	E// [010]
(0,90) (// [001])	III, IV	0.12	I, II, V, VI	$<5\times10^{-3}$	E// [010]
(90,3.2)					
(90,−3.2)	V, VI	0.13	I, II, III, IV	$<5\times10^{-3}$	E// [100]
(90,0) (// [100])	V, VI	0.12	I, II, III, IV	$<5\times10^{-3}$	E// [100]

straints: (i) maximize the branching ratio R; (ii) maximize the absorption, which implies the least number of magnetically nonequivalent classes. In the final step, by choosing the laser polarization, we shall take advantage of the well-defined electric dipole orientation of the $^3H_6(0) \rightarrow {}^3H_4(0)$ transition (Fig. 2) to switch off the classes with poor R value or/and the classes that we did not manage to render magnetically equivalent.

We start by computing the hyperfine splittings, which depend on the orientation (θ, ϕ) of the external magnetic field, by diagonalizing the H_{SH} Hamiltonian both in the ground and the excited states. We then try to find particular values of (θ, ϕ) for which the hyperfine splittings of each class are equal to one another. Because the principal axes of the Λ tensor do not have the same orientation at the $^3H_6(0)$ and $^3H_4(0)$ levels, we need to check that the latter equality holds within both the excited and the ground states. We then compute the branching ratio R for the set of (θ, ϕ) values previously found and then extract the (θ, ϕ) orientation which maximizes the R value.

There is no particular orientation of the magnetic field for which more than two classes can be made magnetically equivalent within both the ground and the excited states. The only situation that satisfies our constraints is to have class I equivalent to class II, class III equivalent to class IV, or class V equivalent to class VI. In those cases, only the external magnetic-field orientations given in Table III lead to a satisfactory branching ratio.

For example (Table III), in the crystallographic frame, for a $(\theta, \phi) = (90°, 3.2°)$ orientation, classes V and VI are equivalent with a branching ratio $R = 0.13$. For this orientation, classes III and IV are equivalent but not classes I and II and all four of them exhibit a poor branching ratio, $R < 5 \times 10^{-3}$. As we can see in Fig. 2 and Table III, classes I, II, III and IV can be switched off by polarizing the laser along the [100] crystallographic direction. If we try to obtain the previously mentioned maximum R value of 0.29, then only one class contributes to the absorption and for classes I, II, III, IV, V, and VI, we find the following external magnetic-field orientations in the crystallographic frame: $(\theta, \phi) = (92.7°, 101.5°)$, $(\theta, \phi) = (87.3°, 78.5°)$, $(\theta, \phi) = (11.8°, 76.7°)$, $(\theta, \phi) = (168.2°, 103.3°)$, $(\theta, \phi) = (101.5°, 2.7°)$, and $(\theta, \phi) = (78.5°, 2.7°)$, respectively.

IV. STARK EFFECT

Interest in the Stark effect of solids was recently renewed thanks to its potential for quantum light storage.[4–6] The influence of static electric field has been studied for decades and was recently reviewed on the celebration of Kaplyanskii's 75th birthday,[18] whose name is closely associated with the pioneer measurements.[19]

In $Tm:Y_2O_3$, we expect to observe a pseudo-Stark splitting.[20] Indeed, as shown in Fig. 2, the different sites with opposite permanent electric dipole orientations undergo opposite Stark shifts under a static electric field. To set the picture, a laser propagating along [100], as well as an electric field along [001], would lift the electric nonequivalency of the sites belonging to classes I and II (opposite shifts). In this case, we observe a splitting into a doublet by hole-burning spectroscopy.[21] This technique can be used to give us a good order of magnitude for the linear Stark coefficient. In order to provide a more accurate measurement, Stark-modulated photon echo was performed.[22] This very sensitive technique makes the coherences of two inverted sites interfere within a two-pulse photon echo. This leads to a modulation of the photon echo intensity as a function of the duration and magnitude of the level splitting induced by a dc electric field (Stark pulse) that is applied in between the two pulses of the echo sequence (see Fig. 4). During the free evolution of the coherences, the application of the Stark pulse induces a differential phase shift between two inverted sites. If, for example, the phase difference is exactly π, these two sites would independently emit echoes that would simply be out of phase. In that case, because of the totally destructive interference, there is no buildup of polarization and no field is radiated after the second light pulse.

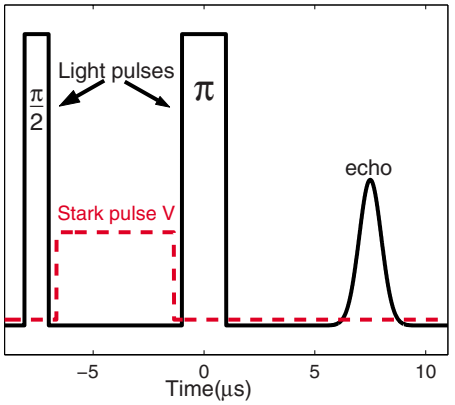

FIG. 4. (Color online) Stark-modulated photon echo. An electric-field pulse in between the optical pulses of a two-pulse photon echo is applied.

In order to apply a static electric field along one crystallographic axis (defined as [001]), we stick a pair of elec-

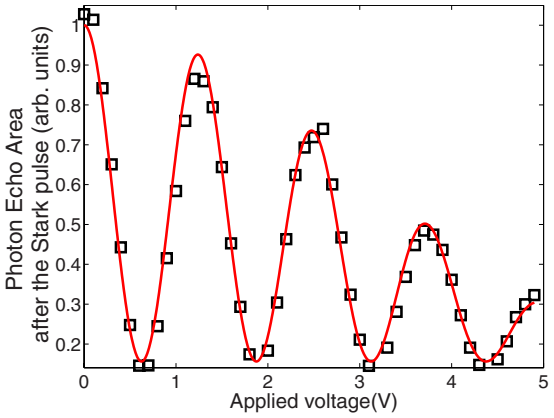

FIG. 5. (Color online) Stark-modulated photon echo as function of the electric-field voltage. The electric field is applied along one crystal axis (defined as [001]); its duration is kept constant at 5.3 μs. We vary the voltage applied on the electrodes and measure the area of the emitted echo. The delay between the two light pulses is 6 μs. The temperature of the sample is 1.2 K. The damping is fitted by a sinc-shape curve (solid red line).

trodes on our orientated crystal separated by 3 mm. We measured the area of the emitted echo as a function of Stark pulse voltage by keeping the duration of the electric pulse constant and varying the applied voltage V (Fig. 5). The oscillation period gives us the frequency difference between the sites with opposite dipoles, which is simply two times the linear Stark shift. We measured an oscillation frequency of 75 kHz/V, which for electrodes separated by 3 mm, gives a Stark coefficient of 22 kHz cm/V. This result should, however, be taken with precaution because of the high dielectric constant (18) of the yttrium oxide host.[23] Indeed, our electrodes are not vapor deposited on the crystal but simply stuck in contact with it, and a tiny gap might thus remain between the electrode and the crystal (hundreds of microns). As a consequence, this would strongly reduce the electric field inside the sample because the air gap thickness multiplied by the dielectric constant is comparable to the electrode spacing. Therefore our measurement gives only a lower bound for the Stark coefficient with a good order of magnitude. The oscillation damping (Fig. 5) can originate from an electric-field inhomogeneity due, for example, to the fringing effect inside a sample of large dielectric constant. To a first approximation, a linear dependency of the field along the propagation axis would lead to a sinc-shape damping curve. This theoretical curve (solid red line in Fig. 5) properly fits the experimental data. The inhomogeneity is then estimated to be around 15% along the sample.

V. CONCLUSION

We showed in this work that $Tm^{3+}:Y_2O_3$ is an interesting candidate for quantum storage application. Indeed, it meets two main requirements toward this goal. First of all, a three-level Λ system can efficiently be tailored in this sample. Second, we experimentally singled out a linear Stark effect on the $^3H_6(0) \rightarrow {}^3H_4(0)$ transition, which is the key element in the protocol relying on controlled and reversible inhomogeneous broadening. To the best of our knowledge, these two properties were never investigated at the same time in a thulium-doped crystal, whose absorbing wavelength is particularly convenient for most of the applications.

To conclude this paper, let us briefly comment on the limited optical coherence time of a few microseconds in this material. Our measurements of a relatively short coherence time in this sample (4 μs at 3 K and 9 μs at 1.2 K by two-pulse photon echo decay) confirmed the results of Sun in p. 403 of Ref. 17. It is an order of magnitude shorter than in the well-studied $Tm^{3+}:YAG$, a fact previously considered as a good reason to reject $Tm^{3+}:Y_2O_3$ for coherent applications. However, in our opinion, this host should be reevaluated in the framework of quantum storage. Indeed, even though the protocol involves the optical coherences as a primary information carrier (direct absorption), a rapid transfer to the Raman coherences allows going beyond the optical dephasing lifetime for the storage. The optical dephasing time should not be considered as an ultimate limitation for our specific application. The ability to perform a Raman transfer is directly related to the presence of a Λ-system between three hyperfine levels.

ACKNOWLEDGMENTS

We thank Jacquet for technical assistance in polishing and orienting the sample used in this work. We would like to thank Pr. R. Cone for discussions and sharing experimental data for comparison.

[1] M. Fleischhauer and M. D. Lukin, Phys. Rev. A **65**, 022314 (2002).
[2] A. V. Turukhin, V. S. Sudarshanam, M. S. Shahriar, J. A. Musser, B. S. Ham, and P. R. Hemmer, Phys. Rev. Lett. **88**, 023602 (2001).
[3] I. D. Abella, N. A. Kurnit, and S. R. Hartmann, Phys. Rev. **141**, 391 (1966).
[4] M. Nilsson and S. Kröll, Opt. Commun. **247**, 393 (2005).
[5] A. L. Alexander, J. J. Longdell, M. J. Sellars, and N. B. Manson, Phys. Rev. Lett. **96**, 043602 (2006).
[6] B. Kraus, W. Tittel, N. Gisin, M. Nilsson, S. Kroll, and J. I. Cirac, Phys. Rev. A **73**, 020302(R) (2006).
[7] J. J. Longdell, E. Fraval, M. J. Sellars, and N. B. Manson, Phys. Rev. Lett. **95**, 063601 (2005).
[8] G. Hétet, J. J. Longdell, A. L. Alexander, P. K. Lam, and M. J. Sellars, Phys. Rev. Lett. **100**, 023601 (2008).
[9] O. Guillot-Noël, Ph. Goldner, E. Antic-Fidancev, and J.-L. Le Gouët, Phys. Rev. B **71**, 174409 (2005).
[10] A. Louchet, J. S. Habib, V. Crozatier, I. Lorgeré, F. Goldfarb, F. Bretenaker, J. L. Le Gouët, O. Guillot-Noël, and P. Goldner, Phys. Rev. B **75**, 035131 (2007).
[11] A. Louchet, Y. Le Du, T. Brouri, F. Bretenaker, T. Chanelière, F. Goldfarb, I. Lorgeré, and J.-L. Le Gouët, Solid State Sci. (to be published).
[12] R. V. Leavitt, J. B. Gruber, N. C. Chang, and C. A. Morrison, J. Chem. Phys. **76**, 4775 (1982).
[13] W. T. Carnall, G. L. Goodman, K. Rajnak, and R. S. Rana, J. Chem. Phys. **90**, 3443 (1989).
[14] B. G. Wybourne, *Spectroscopic Properties of Rare Earths* (Interscience, New York, 1965).
[15] Y. Sun, G. M. Wang, R. L. Cone, R. W. Equall, and M. J. M. Leask, Phys. Rev. B **62**, 15443 (2000).
[16] J. H. Mun, A. Jouini, A. Novoselov, Y. Guyot, A. Yoshikawa, H. Ohta, H. Shibata, Y. Waseda, G. Boulon, and T. Fukuda, Opt. Mater. (Amsterdam, Neth.) **29**, 1390 (2007).
[17] Y. C. Sun, *Rare Earth Materials in Optical Storage and Data Processing Applications Spectroscopic Properties of Rare Earths in Optical Materials*, edited by G. Liu and B. Jacquier (Springer, Berlin, 2005), Chap. 7.
[18] R. M. MacFarlane, J. Lumin. **125**, 156 (2007).
[19] A. Kaplyanskii, J. Lumin. **100**, 21 (2002).
[20] W. Kaiser, S. Sugano, and D. L. Wood, Phys. Rev. Lett. **6**, 605 (1961).
[21] R. M. Shelby and R. M. Macfarlane, Opt. Commun. **27**, 399 (1978).
[22] Y. P. Wang and R. S. Meltzer, Phys. Rev. B **45**, 10119 (1992); A. J. Meixner, C. M. Jefferson, and R. M. Macfarlane, *ibid.* **46**, 5912 (1992).
[23] M. Agarwal, M. R. DeGuire, and A. H. Heuer, Appl. Phys. Lett. **71**, 891 (1997).